

Design of antiferroelectric polarization configuration for ultrahigh capacitive energy storage via increasing entropy

Received: 16 July 2024

Accepted: 10 January 2025

Published online: 18 January 2025



Yongxiao Zhou^{1,2,6}, Tianfu Zhang^{3,6}, Liang Chen^{1,6} , Huifen Yu¹, Ruiyu Wang^{1,4}, Hao Zhang¹, Jie Wu⁵, Shiqing Deng¹, He Qi^{1,5} , Chang Zhou^{1,4}  & Jun Chen^{1,5}

Electric field induced antiferroelectric-ferroelectric phase transition is a double-edged sword for energy storage properties, which not only offers a congenital superiority with substantial energy storage density but also poses significant challenges such as large polarization hysteresis and poor efficiency, deteriorating the operation and service life of capacitors. Here, entropy increase effect is utilized to simultaneously break the long-range antiferroelectric order and locally adjust the fourfold commensurate modulated polarization configuration, leading to a breakthrough in the trade-off between recoverable energy storage density (14.8 J cm^{-3}) and efficiency (90.2%) in medium-entropy antiferroelectrics. The embedding of non-polar phase regions in the incommensurate antiferroelectric matrices, revealing as a mixture of commensurate, incommensurate, and relaxor antiferroelectric polarization configurations, contributes to the diffuse antiferroelectric-ferroelectric phase transition, enhanced phase transition electric field, delayed polarization saturation, and efficient recovery of polarization. This work demonstrates that controlling local diverse antiferroelectric polarization configurations by increasing entropy is an effective avenue to develop high-performance energy storage antiferroelectrics, with implications that can be extended to other materials and functionalities.

Dielectric capacitors have been commercialized for various applications including hybrid electrical vehicles, medical devices, and microwave communications^{1–3}. Compared to batteries, solid oxide fuel cells, and electrochemical capacitors, dielectric capacitors exhibit superiority in terms of ultrahigh power density (P_D), ultrafast discharge rate ($t_{0.9}$), and exceptional operation stability. The low recoverable energy storage density (W_{rec}) of dielectric ceramics, however, greatly restricts their development towards miniaturization and integration.

According to the theory of electrostatic energy storage, the total energy storage density (W_{total}), W_{rec} , and efficiency (η) can be calculated by $W_{\text{total}} = \int_0^{P_{\text{max}}} E dP$, $W_{\text{rec}} = \int_{P_r}^{P_{\text{max}}} E dP$, and $\eta = \frac{W_{\text{rec}}}{W_{\text{total}}}$, respectively, where P_{max} is the maximum polarization, P_r is the remanent polarization, and E is the external electric field (Supplementary Fig. 1). To improve the energy storage performance of dielectrics, extensive efforts are devoted to enhancing P_{max} and breakdown electric

¹Beijing Advanced Innovation Center for Materials Genome Engineering, Department of Physical Chemistry, University of Science and Technology Beijing, Beijing, China. ²School of Materials Science and Engineering, Harbin Institute of Technology, Harbin, China. ³School of Mathematics and Physics, University of Science and Technology Beijing, Beijing, China. ⁴State Key Laboratory for Advanced Metals and Materials, University of Science and Technology Beijing, Beijing, China. ⁵Hainan University, Haikou, Hainan Province, China. ⁶These authors contributed equally: Yongxiao Zhou, Tianfu Zhang, Liang Chen.

✉ e-mail: liangchen@ustb.edu.cn; qiheustb@ustb.edu.cn; changzhou@ustb.edu.cn

field (E_b), decreasing P_r and delaying polarization saturation, simultaneously^{4,5}.

Compared to ferroelectrics (FEs) and relaxor ferroelectrics, anti-ferroelectrics (AFEs) with anti-parallel polarization configuration exhibit reversible AFE-FE phase transition characteristics under external electric fields^{6–8}, leading to the congenital superiority of large polarization fluctuation (high P_{\max} and small P_r) with high W_{rec} . However, the electric-field driven AFE-FE phase transition is usually accompanied by a large difference in the transition electric fields from AFE to FE ($E_{A\rightarrow F}$) and from FE to AFE ($E_{F\rightarrow A}$), which can result in serious polarization hysteresis and energy dissipation (poor η), ultimately degrading the operation and service life of capacitors^{9–12}. To enhance the comprehensive energy storage performance of AFEs, the methods of stabilizing AFE phase by reducing tolerance factor and B-site polarizability, forming relaxor FEs or AFEs by enhancing relaxation behavior to refine domain structure, constructing field-induced multistage phase transition, rolling and spark plasma sintering (SPS) process were adopted, making good progress in PbZrO_3 , PbHfO_3 , AgNbO_3 , and NaNbO_3 systems^{12–19}, especially in PbZrO_3 -based thick films²⁰. Yet the above methods designed in AFE-based ceramics rarely achieved ultrahigh energy storage density ($W_{\text{rec}} \geq 10 \text{ J cm}^{-3}$) and efficiency ($\eta \geq 90\%$), simultaneously.

To develop high-performance dielectric materials, controlling polarization configurations is a fascinating and effective avenue, which directly affects the evolution behavior of macroscopic polarization under external electric fields, while this approach poses great difficulties²¹. Based on the previous regulation understanding of FEs, controlling polymorphic and diverse polarization configuration with multiple magnitudes and angles, in contrast to a single polarization configuration, exhibits significant energy storage advantages in terms of W_{rec} and η , which can be activated by various strategies such as high entropy and supercritical state^{1–3,22,23}. In the case of AFEs, their initial anti-parallel polarization configuration is notably more complex than that of FEs, making efficient regulation of AFE polarization configurations more challenging and with unknown prospects^{24,25}. Generally, as shown in Fig. 1a, AFEs with commensurate modulation polarization structure can produce $1/n$ type superlattice reflections along one axis ($n \geq 4$, n is an integer), exhibiting pronounced AFE-FE phase transition effect with high polarization hysteresis and rapid polarization saturation behaviors²⁰. Making small disturbances in the magnitude and angle of anti-parallel polarization or a partial transition from commensurate to incommensurate modulations ($n \geq 4$, n is a non-integer) can form field-induced multistage phase transition, which can largely improve W_{rec} (Fig. 1b)^{12,20,26–28}. However, the intense AFE-FE phase

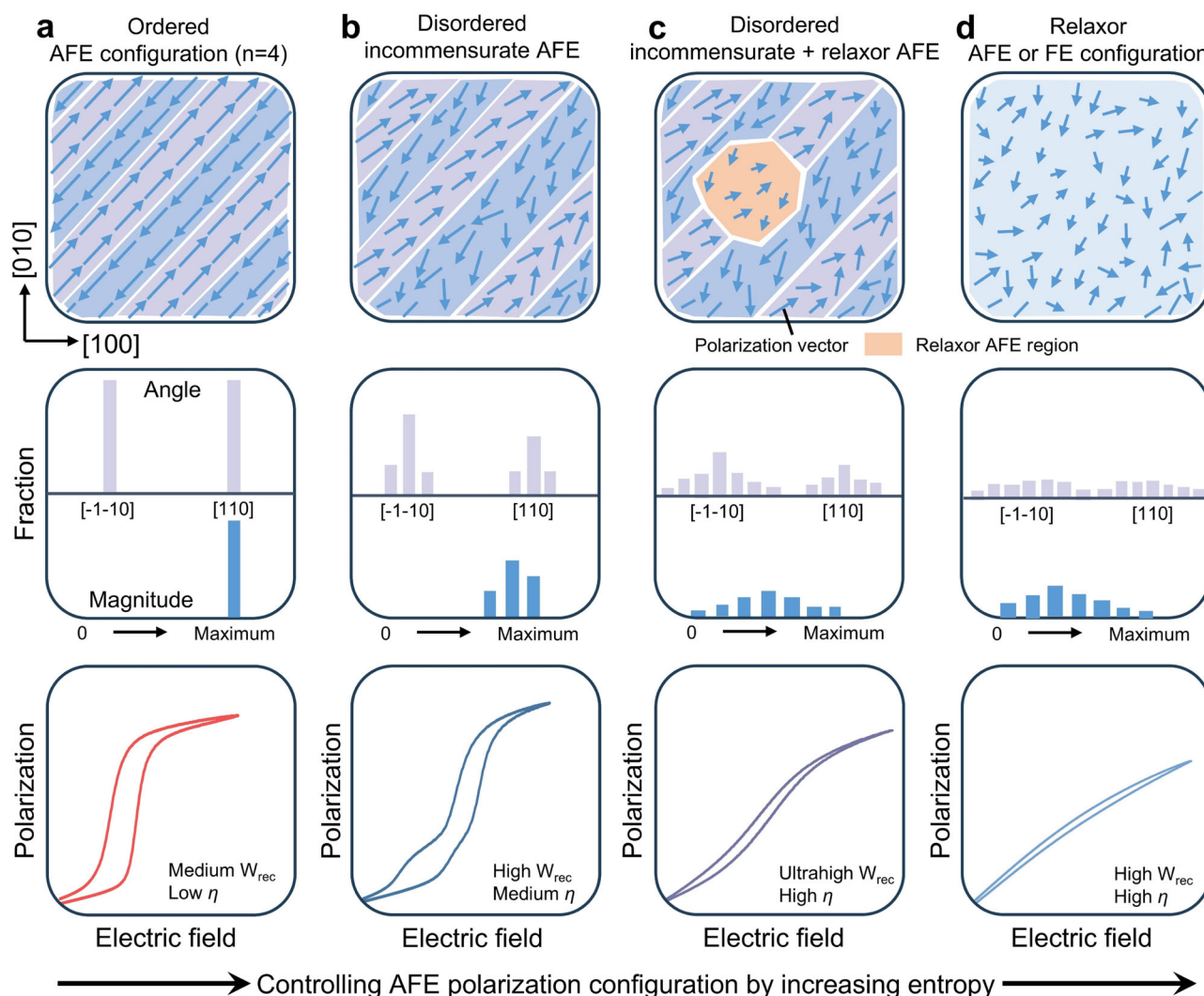


Fig. 1 | Schematic diagram for controlling AFE polarization configuration by increasing entropy. Polarization configuration with the corresponding polarization angle and magnitude distribution as well as P - E loop in the **a** ordered

commensurate AFE ($n = 4$), **b** disordered incommensurate AFE, **c** mixture of disordered incommensurate and relaxor AFE, **d** relaxor AFE or FE.

transition has not been eliminated, leading to a medium η and poor working stability.

To improve the overall energy storage properties, in this work, entropy increase effect is proposed to control AFE polarization configurations. A new $\text{Pb}(\text{Zr}_{1/3}\text{Sn}_{1/3}\text{Hf}_{1/3})\text{O}_3$ AFE component with an ordered commensurate AFE polarization configuration is chosen as the matrix. To preserve AFE features and efficiently control polarization as much as possible, La with higher valence state and smaller radius than Pb is introduced to form $(\text{Pb}_{1-3/2x}\text{La}_x)(\text{Zr}_{1/3}\text{Sn}_{1/3}\text{Hf}_{1/3})\text{O}_3$ (PLxZSH) solid solutions. It is imperative to establish a diverse AFE polarization configuration with the wide-ranging distribution of polarization angles and magnitudes between adjacent stripes, which possess varying potential barriers for polarization switching, resulting in the smooth polarization rising and recovery paths under external electric fields (Fig. 1c). It should be noted that excessive perturbation of polarization to form highly disordered polarization configurations by establishing high-entropy state may cause a significant decrease in P_{max} and W_{rec} , which can be attributed to the obvious disappearance of AFE configuration accompanied by a downward concave P - E loop transforming into an upward convex one, although η can be further improved (Fig. 1d). As a result, we successfully design a local diverse AFE polarization configuration with the coexisting commensurate, incommensurate, and relaxor AFE polarization configurations using entropy increase effect by introducing an appropriate amount of La (Fig. 1c), realizing outstanding energy storage properties in incommensurate medium-entropy AFEs, which exhibit enormous application potential for advanced capacitors.

Results and discussion

Energy storage performance by increasing entropy

We prepare a series of medium-entropy components PLxZSH ($x = 0, 0.02, 0.04, 0.06$) with configurational entropy (ΔS_{config}) spanning from 1.10 R to 1.46 R to explore energy storage properties from low electric field until breakdown. As shown in Fig. 2a and Supplementary Fig. 2, the unipolar P - E loops with perfect AFE-FE phase transition

characteristics can be obviously found in PLOZSH ceramic. As entropy increases, field-induced multistage phase transition emerges in PLO.02ZSH and PLO.04ZSH ceramics, further evolving into a diffuse AFE-FE phase transition in PLO.06ZSH ceramic with smooth polarization rise and recovery paths under external electric fields. The above phase transition behaviors can also be verified by the change in current density under external electric fields, which are manifested as gradually decreasing and diffusing current density peaks as La increases (Fig. 2b). All samples exhibit a typical orthorhombic phase perovskite structure, revealing as the splitting of (200) diffraction peak, at room temperature without any second phase (Supplementary Fig. 3-4). Importantly, based on the above results, the temperature-dependent dielectric spectrum gradually broadens with increasing La (Supplementary Fig. 5), indicating that the macroscopic AFE nature of the PLxZSH samples are always maintained. It should be noted that $E_{\text{A-F}}$, $E_{\text{F-A}}$, and E_{b} also increase with increasing La content. As a result, a small W_{rec} of 6.5 J cm^{-3} with a low η of 67.9% can be achieved in PLOZSH AFE ceramic, which can be significantly improved to realize an ultrahigh W_{rec} of 16.3 J cm^{-3} with a high η of 81.2% in medium-entropy PLO.06ZSH sample by increasing entropy for enhancing local random field and breaking long-range AFE order (Fig. 2c, d).

To further develop the capacitive energy storage potential of medium-entropy PLO.06ZSH sample, SPS is employed to optimize the internal structure quality. As presented in Fig. 2e, the polarization rise and recovery paths shown in the P - E loops of SPS optimized PLO.06ZSH sample (SPS-PL0.06ZSH) are noticeably smoother than that of PLO.06ZSH ceramic with smaller hysteresis and P_r , which is also accompanied by a higher E_{b} of 86 kV mm^{-1} . The outstanding comprehensive energy storage properties with an ultrahigh W_{rec} of 14.8 J cm^{-3} and a gratifying η of 90.2% can be realized in SPS-PL0.06ZSH ceramic (Fig. 2f). As summarized in Fig. 2g and Supplementary Fig. 6, compared to other dielectric systems, the ultrahigh W_{rec} reported in our work stands at the forefront, especially with a super high η exceeding 90%, showcasing the optimal overall energy storage performance among AFE ceramics, encompassing both lead-based and lead-free systems.

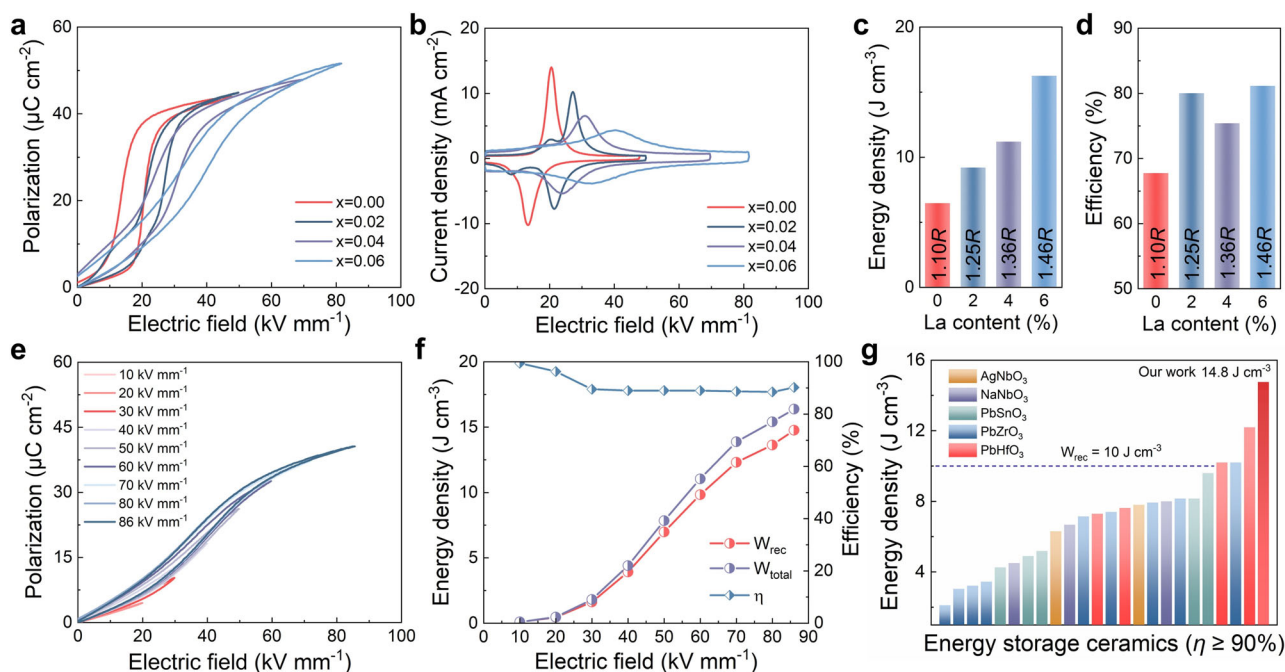


Fig. 2 | Energy storage performance of PLxZSH ceramics. **a** P - E loops and **b** J - E loops measured at E_{b} for PLxZSH ceramics. **c** W_{rec} and **d** η as a function of La content with different entropy values for PLxZSH ceramics. **e** P - E loops under different electric fields of SPS-PL0.06ZSH ceramic. **f** W_{total} , W_{rec} and η as a function of

electrical field for SPS-PL0.06ZSH ceramic. **g** Comparisons of W_{rec} ($\eta \geq 90\%$) between our work and other AFE bulk ceramics. The references are provided in Supplementary Table 1.

Structural origins of superior energy storage performance

The superior energy storage properties can be attributed to the enhanced breakdown property, large polarization fluctuation and delayed polarization saturation. All samples exhibit dense microstructure and the average grain size (G_a) of PLOZSH, PLO.02ZSH, PLO.04ZSH, and PLO.06ZSH is 0.95, 2.14, 1.62, and 1.19 μm , respectively, which significantly reduces to 0.25 μm in the SPS-PLO.06ZSH ceramic (Supplementary Fig. 7–8). The decreased G_a serves as a vital external contribution to improve E_b by increasing the density of high-resistance grain boundaries, which can hinder the migration of charge carriers under external electric fields. To further reveal the origin of high E_b , phase-field simulation using finite element methods with 2D models are processed in PLOZSH, PLO.06ZSH, and SPS-PLO.06ZSH samples to simulate the reliable dielectric breakdown processes, which concurrently account for both the intrinsic property (dielectric constant) and external structure characteristics (grain and grain boundary distribution), simultaneously (Supplementary Fig. 9)²⁹. As shown in Fig. 3a, compared to other samples, the electric tree first penetrates the entire PLOZSH ceramic, indicating the lowest breakdown field. Subsequently, PLO.06ZSH undergoes breakdown, and at this time, the electrical tree of SPS-PLO.06ZSH only propagates about 70% accompanied by shorter branches. It is known that the strong electric field is

concentrated in grain boundaries. At the brink of breakdown, the electric field distribution of SPS-PLO.06ZSH is more uniform, avoiding the occurrence of high local electric fields and premature breakdown (Fig. 3b).

The dense and uniform grain structure without any voids can also be obviously found in PLOZSH and PLO.06ZSH ceramics by transmission electron microscope (TEM) (Fig. 3c, g). According to the result of selected area electron diffraction (SAED) shown in Fig. 3d, PLOZSH ceramic exhibits a 4-fold commensurate modulation AFE structure revealed by the satellite spots of $(110)/4$. Furthermore, the stripe structure can be observed in PLOZSH ceramic with the width of 1.22–1.29 nm by high-resolution TEM (HR-TEM), which is composed of 4 unit cells along $[110]_c$ axis (Fig. 3e). For PLO.06ZSH sample, the incommensurate modulation AFE structure can be demonstrated by the satellite spots of about $(110)/4.5$ (Fig. 3h). However, no stripes but porphyritic morphology can be obtained through HR-TEM and inverse Fourier transform (Fig. 3i and Supplementary Fig. 10), indicating that the long-range ordered AFE polarization configuration is disrupted by doping La to increase entropy while the commensurate structure transitions to the incommensurate structure³⁰. As present in Fig. 3f, j, the HR-TEM images of lattice fringes and SAED patterns in both medium-entropy PLOZSH and PLO.06ZSH ceramics exhibit a good

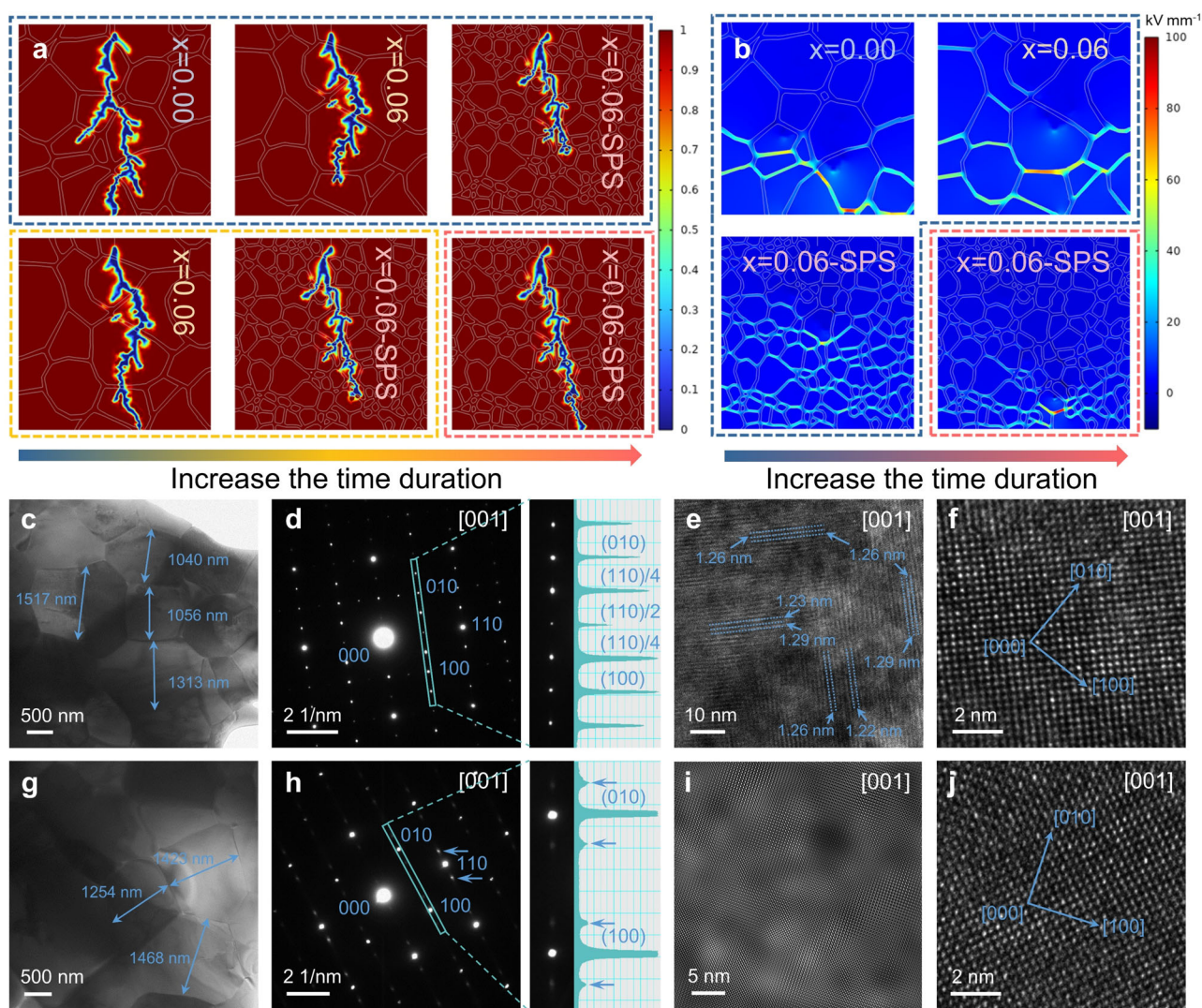


Fig. 3 | Breakdown simulation and domain structure of PLxZSH ceramics.

Phase-field simulation of **a** breakdown path distribution or electrical tree evolution (rectangular frames with the same color represent the same time duration) and **b** electric field distribution for PLxZSH ceramic. **c** TEM image of grains, **d** SAED

pattern, **e** HR-TEM pattern of domain morphology, and **f** atomic image of PLOZSH ceramic along $[001]_c$. **g** TEM image of grains, **h** SAED pattern, **i** HR-TEM pattern of domain morphology through inverse Fourier transform, and **j** atomic image of PLO.06ZSH ceramic.

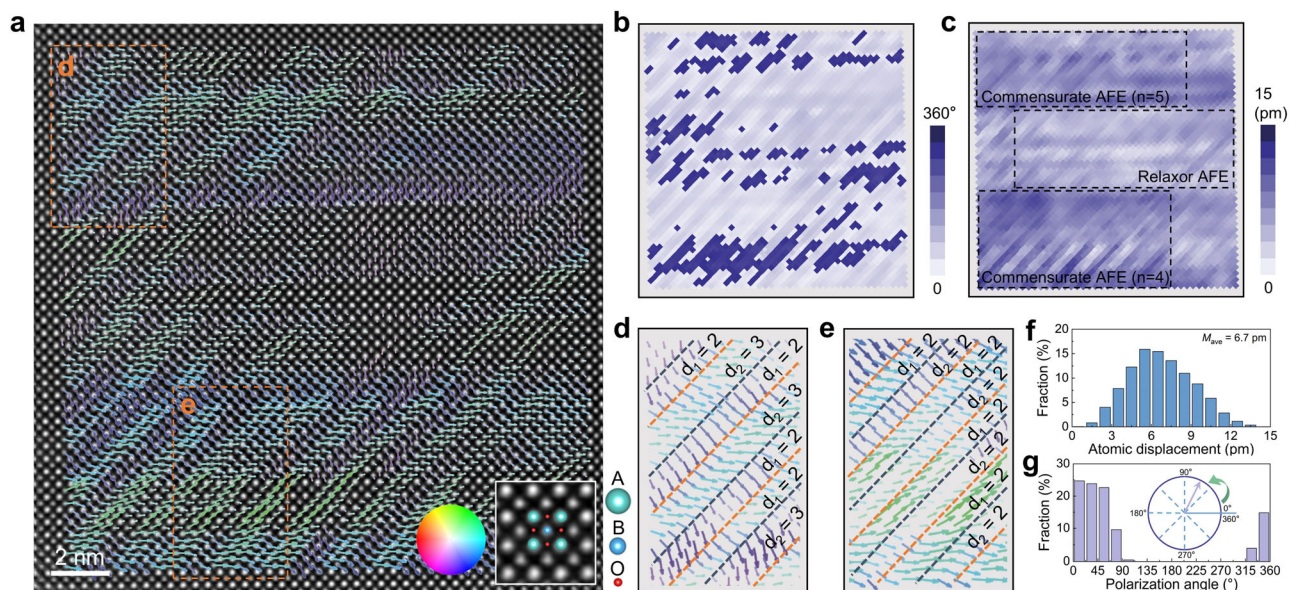


Fig. 4 | Local polarization of PLO.06ZSH ceramic. **a** Atomic-resolution HAADF image and the corresponding local atomic (cation) displacement vectors along $[001]_c$. **b** Polarization angle, and **c** atomic displacement mapping along $[001]_c$. The preferential commensurate modulation with **d** $n = 5$ and **e** $n = 4$ found in the orange

rectangle of **a** d_1 and d_2 are used to distinguish adjacent stripes within a modulation period. The statistic of calculated **f** local atomic displacement, and **g** polarization angle distribution along $[001]_c$.

crystalline quality without any impure phase. Furthermore, to further reveal the information of oxygen octahedral tilts, atomic-resolution annular bright-field transmission electron microscope (ABF-TEM) is conducted in PLO.06ZSH ceramic (Supplementary Fig. 11). The weak oxygen octahedral distortion with extremely small average tilt angles of clockwise (0.63°) and anticlockwise (-0.51°) can be discovered, exhibiting random rather than long-range ordered distribution behavior. These behaviors can contribute to the large improvement of η , reducing energy dissipation during electric field loading and unloading processes^{20,31}.

Atomic-scale analysis of local polarization configuration

To deeply understand the structural origins of excellent energy storage performance, atomic-resolution high-angle annular dark-field scanning transmission electron microscope (HAADF-STEM) is performed in medium-entropy PLO.06ZSH ceramic to analyze the local polarization configuration from the perspective of cation displacement. As shown in Fig. 4a, it is obvious that the wave-like polarization fluctuations with different colors signifying different polarization angles along the $[110]_c$ axis can be achieved by 2D Gaussian peak fitting based on the structural features of perovskite unit cell²¹, which contribute to the nanoscale stripes composed of polarization segments in different directions (Fig. 4b, g). Compared to AFEs with polarization configurations in an antiparallel arrangement (180°) or a nearly orthogonal arrangement (90°) in adjacent stripes, the angles between adjacent stripes in this work are smaller, which vary in a wide range from 0° to about 70° ^{6,7,32}. It should be noted that the disappearing stripe structure in PLO.06ZSH ceramic is mainly attributed to the small angles between adjacent stripes, which cannot be effectively distinguished in HR-TEM. It is known that polarization magnitudes can be measured by local atomic displacements in (anti)ferroelectrics²⁶. As described in Fig. 4c, f, the local atomic displacements between adjacent stripes are also not equal, which vary from 0 to 15 pm over a wide range. The wide-ranging distribution of polarization angles and magnitudes between adjacent stripes establishes diverse configurations of local AFE nanoregions, leading to the smooth polarization rising and recovery paths under external electric fields owing to their different potential barriers for polarization switching. The smooth P - E loops can

eliminate the sudden changes in volume and internal stress caused by AFE-FE phase transition, significantly reducing the possibility of electromechanical breakdown and enhancing E_b of the AFE-based dielectrics. Moreover, the enhanced P_m can also be achieved at low electric fields with increasing La (Supplementary Fig. 12), benefiting from that the long-range ordered AFE configuration is gradually broken by increasing entropy to yield more low-energy barrier polarization configurations, which can be driven by low electric fields.

It is recognized that the incommensurate modulation structure is actually the average effect over an ensemble of stripes (or a mixture) of commensurate modulations²⁷. Interestingly, the preferential commensurate modulations with $n = 5$ ($n = d_1 + d_2$) and $n = 4$ can be clearly found in Fig. 4d, e, respectively, which cause the incommensurate modulation AFE structure with the satellite spots of about $(110)/4.5$. It should be noted that there are also a portion of local incommensurate modulation polarization structures in the above two types of commensurate regions (Fig. 4a, c). The AFE region with extremely small local displacements can also be observed, which can be considered as relaxor AFE. To study the source of the different AFE polarization configuration regions, the intensity of A-site and B-site atomic columns is identified separately in Supplementary Fig. 13, which is positively correlated with atomic number (Z). It should be noted that intensity distribution of B-site atomic columns is more disordered than that of A-site atomic columns in this work and the polarization structure of lead-based AFE has been widely reported to be mainly dominated by A-site^{6,26,32}. We mainly analyze the intensity distribution of A-site atomic columns. Obviously, the high-intensity and low-intensity A-site atomic columns are found to be concentrated in the commensurate modulation structures with $n = 4$ and $n = 5$, respectively, which can be speculated that La concentrated in commensurate modulation structures with $n = 5$ and a small amount of La distributed in commensurate modulation structures with $n = 4$ because Z_{La} is much smaller than Z_{Pb} . A more chaotic intensity distribution exists in the relaxor AFE region, indicating higher component disorder, which is an important cause of relaxation^{33,34}. Therefore, the introduction of La promotes not only the transition of the modulation period, but also the generation of relaxation behavior, which can adjust the polarization angle and magnitude, contributing to diverse local AFE polarization

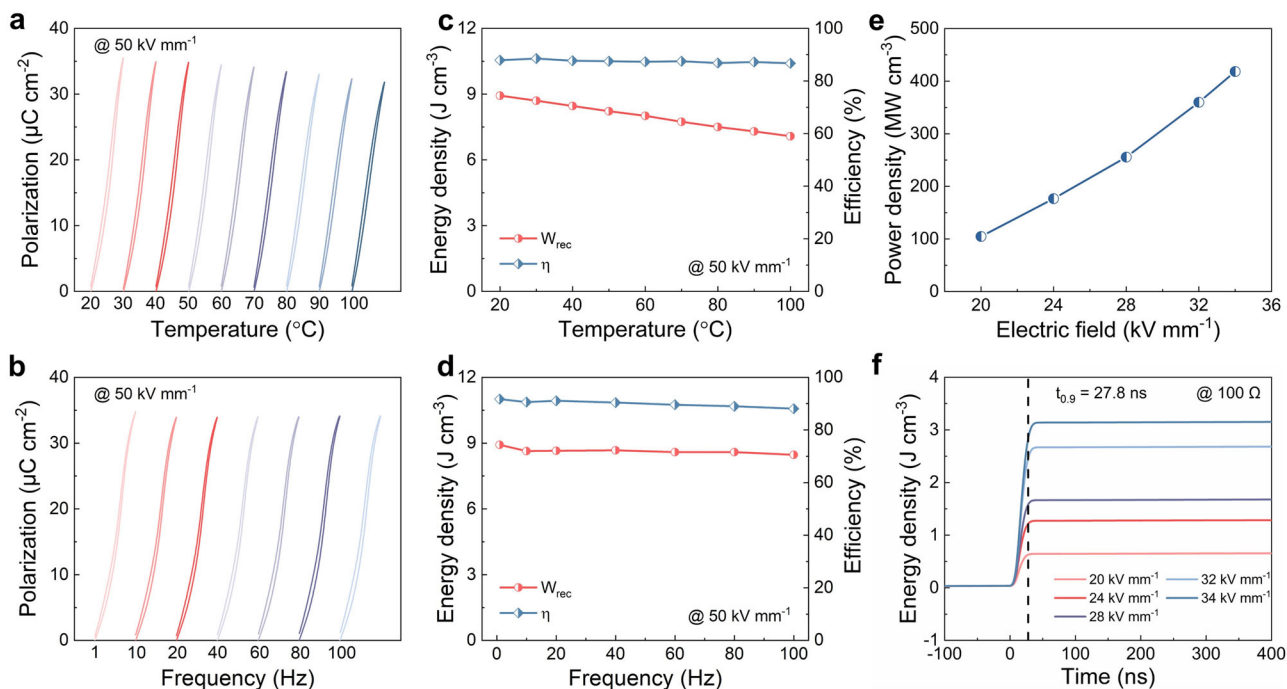


Fig. 5 | Stability and charge/discharge performance of PL0.06ZSH ceramic. a P - E loops under different temperatures at 50 kV mm⁻¹. **b** P - E loops under different frequencies at 50 kV mm⁻¹. **c** W_{rec} and η as a function of temperature at 50 kV mm⁻¹.

d W_{rec} and η as a function of frequency at 50 kV mm⁻¹. **e** P_D as a function of electric field. **f** W_D as a function of electric field.

configurations. Firstly, the preserved AFE polarization configuration characteristics with the wide-ranging distribution of polarization angles and magnitudes can generate diffusive AFE-FE phase transitions under external electric fields, contributing to a large P_m and a small P_r , simultaneously. Secondly, combining with a small amount of near-zero local atomic displacements in commensurate/incommensurate AFE polarization configurations, the relaxor AFE region with large random fields can also provide a restoring force to promote polarization in commensurate/incommensurate regions to quickly and efficiently return to its initial state when removing the electric field, resulting in low-hysteresis P - E loops with small P_r and high η . Thirdly, based on the AFE structure with low n and large random fields in relaxor AFE region, E_{A-F} and E_{F-A} can also be largely enhanced by the diverse AFE polarization configurations and relaxation driven delayed polarization saturation behaviors²⁶. Consequently, the outstanding comprehensive energy storage properties can be realized in La modified medium-entropy lead-based AFE ceramics by forming local diverse AFE polarization configurations.

Stability and charge/discharge properties

The thermal, frequency, and cycling stability of energy storage properties play an important role in advanced capacitor applications. As shown in Fig. 5a, the temperature-dependent unipolar P - E loops of medium-entropy PL0.06ZSH ceramic are tested from 20 °C to 100 °C at 50 kV mm⁻¹, which are slim with low hysteresis and nearly unchanged P_m . High W_{rec} of 8.0 ± 0.9 J cm⁻³ and high η of $87.6 \pm 0.9\%$ can be well maintained, testifying to the exceptional thermal stability owing to the temperature-insensitive phase structure and dielectric loss from room temperature to 100 °C (Fig. 5c and Supplementary Fig. 5 and 14). Regarding frequency stability, the slender unipolar P - E loops over a wide range from 1 to 100 Hz can be obtained in the studied sample under 50 kV mm⁻¹, presenting remarkable frequency-independent energy storage performance (W_{rec} - 8.7 ± 0.2 J cm⁻³ and η - $89.9 \pm 1.8\%$) (Fig. 5b, d). Furthermore, the P - E loops of PL0.06ZSH ceramic remain slim with small polarization hysteresis even after 10^6 cycles under an

electric field of 50 kV mm⁻¹, which sustains a high W_{rec} of 9.9 ± 0.1 J cm⁻³ with an impressive η of $88.1 \pm 1.8\%$ in the whole process, indicating the superior cycling stability (Supplementary Fig. 15).

The assessment of the energy storage application potential necessitates the consideration of the charge/discharge performance as a pivotal metric^{31,35}. Within the context of PL0.06ZSH ceramic, the presence of regularly oscillating underdamped waveforms under the influence of external electric fields is unambiguously discernible (Supplementary Fig. 16a). This phenomenon triggers a pronounced escalation in P_D , surging from 105 to 418 MW cm⁻³, as the electric field intensifies from 20 to 34 kV mm⁻¹ (Fig. 5e). Furthermore, the overdamped discharge process, when subjected to electric fields ranging from 20 to 34 kV mm⁻¹ with different resistors of 100, 200, and 300 Ω, exhibits stable waveforms and properties (Supplementary Fig. 16b–i). Notably, a remarkable discharge energy density (W_D) of approximately 3.2 J cm⁻³ can be discharged to 90% within an exceptionally brief duration of ~27.8 ns at 34 kV mm⁻¹ under a load resistance of 100 Ω (Fig. 5f). These remarkable findings underscore the exceptional comprehensive performance of the investigated ceramics, thereby portending a promising future for their application in energy storage capacitors.

In summary, harnessing the entropy increase phenomenon, we have meticulously crafted a locally heterogeneous AFE polarization landscape, where commensurate, incommensurate, and relaxor AFE polarization configurations intertwine harmoniously. This intricate arrangement facilitates the traversal of seamless polarization trajectories, characterized by minimal hysteresis, pronounced polarization fluctuations, and delayed polarization saturation. Consequently, we have achieved groundbreaking overall energy storage properties, accompanied by an ultrahigh W_{rec} of 14.8 J cm⁻³ and an exemplary η of 90.2%, within the realm of AFE ceramics. It is believed that this work demonstrates an effective strategy of controlling local diverse AFE polarization configurations through increasing entropy to develop new antiferroelectrics with excellent energy storage performance, which is expected to attract broad research interests and be expanded to other fields.

Methods

Sample preparation

(Pb_{1-3/2x}La_x)(Zr_{1/3}Sn_{1/3}Hf_{1/3})O₃ ($x = 0, 0.02, 0.04$, and 0.06) (Abbreviated as PLxZSH) ceramics were fabricated by traditional solid-state reaction and SPS methods. PbO (Aladdin, 99.9%), La₂O₃ (Aladdin, 99.99%), ZrO₂ (Aladdin, 99.99%), HfO₂ (Aladdin, 99.9%) and SnO₂ (Aladdin, 99.5%) were used as the started materials. The stoichiometric powders were mixed with alcohol and yttrium stabilized zirconia balls in nylon jars for 12 h at 400 rpm by planetary ball mill. The mixed powders were dried at 90 °C for 3 h and then calcined at 800 °C for 2 h. Then the calcined powder was mixed with 0.8 wt% polyvinyl butyral (PVB) binder by high-energy ball milling with alcohol at 600 rpm for 12 h again. After drying at 90 °C for 3 h, the mixed powders were pressed into pellets with a diameter of 10 mm under 300 MPa. The pellets were heated to 550 °C for removing PVB blinder and then sintered at 1220 °C for 2 h. Besides, PLZSH-0.06 was further prepared by SPS method. The mixed powders after high-energy ball milling were poured into a graphite mold of 10 mm with graphite paper protection. Then the graphite mold was pressed into the furnace chamber at a pressure of 60 MPa and vacuumed to 1×10^{-3} Pa. The sintering process is divided into three steps: first, the sample was heated to 850 °C with 100 °C min⁻¹; second, the sample was heated to 900 °C with 25 °C min⁻¹; finally, the sample was sintered at 900 °C for 7 min. The SPS-prepared samples were annealed at 830 °C for 10 h to remove carbon. The sintered ceramics were polished to a thickness of 50–80 μm for electrical property tests. The parallel surfaces of ceramics were coated with silver electrodes with an area of 0.8 mm² (1 mm in diameter) and fired at 550 °C for 20 min.

Structure characterizations

Room-temperature and temperature-dependent X-ray diffraction patterns were tested using an X-ray diffractometer (X'pert PRO, PANalytical, the Netherlands) with Cu K α radiation ($\lambda = 1.54$ Å). Slow scanning room-temperature X-ray diffraction patterns for Rietveld refinement were tested using an X-ray diffractometer (Rigaku) with Co target ($\lambda = 1.79$ Å). The morphologies and element distribution maps of grains were characterized by scanning electron microscope (LEO1530, ZEISS SUPRA 55, Oberkochen, Germany). The TEM samples were polished to 30 μm and then thinned by an ion milling system (PIPS, Model 691, Gatan Inc., Pleasanton, CA, USA). TEM was used to observe the grain distribution, domain morphology and SAED by a field-emission TEM (JEM-2100F, JEOL, Japan). STEM (aberration-corrected FEI Titan Cubed Themis G2 300) was applied to obtain the HAADF atomic-scale images. STEM (Cs-corrected Hitachi HF5000) was applied to obtain the ABF atomic-scale images. The precise atomic positions in STEM images were elucidated through 2D Gaussian fitting. The polarization vectors and oxygen octahedral tilts were calculated and extracted through customized MATLAB scripts.

Electrical performance measurements

The room-temperature, temperature, frequency, and cycling-dependent P - E loops were measured using a ferroelectric analyzer (aix ACCT, TF Analyzer 1000, Aachen, Germany). A precision LCR meter (Keysight E4990A, Santa Clara, CA, USA) was applied to obtain the temperature-dependent and frequency-dependent dielectric performance. The charge/discharge performance of samples were tested by a commercial charge-discharge platform (CFD-003, Gogo Instruments Technology, Shanghai, China).

Phase-Field Simulation

The simulation results of dielectric breakdown process were simulated by finite element methods with 2D models using COMSOL software. The details can be found in the Supplementary Information.

Data availability

All data supporting this study and its findings are available within the article and its Supplementary Information. The data that support the findings of this study are available from the corresponding author upon reasonable request.

References

- Pan, H. et al. Ultrahigh-energy density lead-free dielectric films via polymorphic nanodomain design. *Science* **365**, 578–582 (2019).
- Zhang, M. et al. Ultrahigh energy storage in high-entropy ceramic capacitors with polymorphic relaxor phase. *Science* **384**, 185–189 (2024).
- Chen, L. et al. Giant energy-storage density with ultrahigh efficiency in lead-free relaxors via high-entropy design. *Nat. Commun.* **13**, 3089 (2022).
- Yang, L. et al. Perovskite lead-free dielectrics for energy storage applications. *Prog. Mater. Sci.* **102**, 72–108 (2019).
- Wang, G. et al. Electroceramics for high-energy density capacitors: current status and future perspectives. *Chem. Rev.* **121**, 6124–6172 (2021).
- Ma, T. et al. Uncompensated polarization in incommensurate modulations of perovskite antiferroelectrics. *Phys. Rev. Lett.* **123**, 217602 (2019).
- Fan, Z. et al. TEM investigation of the domain structure in PbHfO₃ and PbZrO₃ antiferroelectric perovskites. *J. Mater. Sci.* **55**, 4953–4961 (2020).
- Randall, C. A., Fan, Z., Reaney, I., Chen, L. Q. & Trolier-McKinstry, S. Antiferroelectrics: History, fundamentals, crystal chemistry, crystal structures, size effects, and applications. *J. Am. Ceram. Soc.* **104**, 3775–3810 (2021).
- Jiang, J. et al. Ultrahigh energy storage density in lead-free relaxor antiferroelectric ceramics via domain engineering. *Energy Storage Mater.* **43**, 383–390 (2021).
- Qi, H. et al. Ultrahigh energy-storage density in NaNbO₃-based lead-free relaxor antiferroelectric ceramics with nanoscale domains. *Adv. Funct. Mater.* **29**, 1903877 (2019).
- Chen, C. et al. Synergistic optimization of energy storage density of PYN-based antiferroelectric ceramics by composition design and microstructure engineering. *Small* **19**, 2302376 (2023).
- Meng, X., Zhao, Y., Li, Y. & Hao, X. Simultaneously achieving ultrahigh energy density and power density in PbZrO₃-based antiferroelectric ceramics with field-induced multistage phase transition. *J. Alloys Compd.* **868**, 159149 (2021).
- Zhao, L., Liu, Q., Gao, J., Zhang, S. & Li, J. F. Lead-free antiferroelectric silver niobate tantalate with high energy storage performance. *Adv. Mater.* **29**, 1701824 (2017).
- Luo, N. et al. Constructing phase boundary in AgNbO₃ antiferroelectrics: pathway simultaneously achieving high energy density and efficiency. *Nat. Commun.* **11**, 4824 (2020).
- Xie, A. et al. NaNbO₃-(Bi_{0.5}Li_{0.5})TiO₃ lead-free relaxor ferroelectric capacitors with superior energy-storage performances via multiple synergistic design. *Adv. Energy Mater.* **11**, 2101378 (2021).
- Wang, X. et al. Ultrahigh energy storage density and efficiency in PLZST antiferroelectric ceramics via multiple optimization strategy. *J. Eur. Ceram. Soc.* **43**, 4051–4059 (2023).
- Chao, W., Tian, L., Yang, T., Li, Y. & Liu, Z. Excellent energy storage performance achieved in novel PbHfO₃-based antiferroelectric ceramics via grain size engineering. *Chem. Eng. J.* **433**, 133814 (2022).
- Tan, H. et al. SPS prepared NN-24SBT lead-free relaxor-antiferroelectric ceramics with ultrahigh energy-storage density and efficiency. *Scripta Mater.* **210**, 114428 (2022).

19. Wang, H., Liu, Y., Yang, T. & Zhang, S. Ultrahigh energy-storage density in antiferroelectric ceramics with field-induced multiphase transitions. *Adv. Funct. Mater.* **29**, 1807321 (2019).
20. Ge, G. et al. Tunable domain switching features of incommensurate antiferroelectric ceramics realizing excellent energy storage properties. *Adv. Mater.* **34**, 2201333 (2022).
21. Chen, L. et al. Near-zero energy consumption capacitors by controlling inhomogeneous polarization configuration. *Adv. Mater.* **36**, 2313285 (2024).
22. Chen, L. et al. Local diverse polarization optimized comprehensive energy-storage performance in lead-free superparaelectric. *Adv. Mater.* **34**, 2205787 (2022).
23. Xie, A. et al. Supercritical relaxor nanograined ferroelectrics for ultrahigh-energy-storage capacitors. *Adv. Mater.* **34**, 2204356 (2022).
24. Zhuo, F. et al. Perspective on antiferroelectrics for energy storage and conversion applications. *Chin. Chem. Lett.* **32**, 2097–2107 (2021).
25. Wei, X. K. et al. An unconventional transient phase with cycloidal order of polarization in energy-storage antiferroelectric PbZrO₃. *Adv. Mater.* **32**, 1907208 (2020).
26. Fu, Z. et al. Unveiling the ferrielectric nature of PbZrO₃-based antiferroelectric materials. *Nat. Commun.* **11**, 3809 (2020).
27. Tan, X., Ma, C., Frederick, J., Beckman, S. & Webber, K. G. The antiferroelectric \leftrightarrow ferroelectric phase transition in lead-containing and lead-free perovskite ceramics. *J. Am. Ceram. Soc.* **94**, 4091–4107 (2011).
28. Lu, Y. et al. Multistage phase transition induced excellent capacitive energy storage performances in (Pb,La,Sr)(Zr,Sn)O₃ antiferroelectric ceramics. *Ceram. Int.* **49**, 37881–37887 (2023).
29. Chen, L. et al. Large energy capacitive high-entropy lead-free ferroelectrics. *Nano-Micro Lett.* **15**, 65 (2023).
30. Fu, D., Taniguchi, H. & Itoh, M. *Phys. Rev. Lett.* **103**, 207601 (2009).
31. Qi, H. et al. Large (anti)ferrodistortive NaNbO₃-based lead-free relaxors: polar nanoregions embedded in ordered oxygen octahedral tilt matrix. *Mater. Today* **60**, 91–97 (2022).
32. Jiang, R.-J. et al. Atomic insight into the successive antiferroelectric-ferroelectric phase transition in antiferroelectric oxides. *Nano Lett.* **23**, 1522–1529 (2023).
33. Bokov, A. & Ye, Z.-G. Recent progress in relaxor ferroelectrics with perovskite structure. *J. Mater. Sci.* **41**, 31–52 (2006).
34. Li, F., Zhang, S., Damjanovic, D., Chen, L. Q. & Shrout, T. R. Local structural heterogeneity and electromechanical responses of ferroelectrics: learning from relaxor ferroelectrics. *Adv. Funct. Mater.* **28**, 1801504 (2018).
35. Zhao, P., Li, L. & Wang, X. BaTiO₃-NaNbO₃ energy storage ceramics with an ultrafast charge-discharge rate and temperature-stable power density. *Microstructures* **3**, 2023002 (2023).

Acknowledgements

This work was supported by the National Key R&D Program of China (grant no. 2023YFB3508200), the National Natural Science Foundation of China (grant nos. 22235002, 52172181, 22205016, and 52302133), the

China National Postdoctoral Program for Innovative Talents (grant no. BX20230040), and the China Postdoctoral Science Foundation (grant no. 2023M740208).

Author contributions

This work was conceived and designed by L.C., H.Q., and C.Z. Y.Z. and T.Z. fabricated the samples, tested the energy storage, dielectric, structure, stability and other properties, and processed related data, assisted by L.C. The finite element simulation was processed by H.Y. The XRD and dielectric spectra were collected by R.W., H.Z., and J.W. The SEM images were filmed and processed by Y.Z. The TEM and STEM images were filmed and processed by L.C. and S.D. The manuscript was drafted by Y.Z. and L.C., revised by H.Q., C.Z., and J.C. All authors participated in the data analysis and discussions.

Competing interests

The authors declare no competing interests.

Additional information

Supplementary information The online version contains supplementary material available at <https://doi.org/10.1038/s41467-025-56194-1>.

Correspondence and requests for materials should be addressed to Liang Chen, He Qi or Chang Zhou.

Peer review information *Nature Communications* thanks the anonymous reviewer(s) for their contribution to the peer review of this work. A peer review file is available.

Reprints and permissions information is available at <http://www.nature.com/reprints>

Publisher's note Springer Nature remains neutral with regard to jurisdictional claims in published maps and institutional affiliations.

Open Access This article is licensed under a Creative Commons Attribution-NonCommercial-NoDerivatives 4.0 International License, which permits any non-commercial use, sharing, distribution and reproduction in any medium or format, as long as you give appropriate credit to the original author(s) and the source, provide a link to the Creative Commons licence, and indicate if you modified the licensed material. You do not have permission under this licence to share adapted material derived from this article or parts of it. The images or other third party material in this article are included in the article's Creative Commons licence, unless indicated otherwise in a credit line to the material. If material is not included in the article's Creative Commons licence and your intended use is not permitted by statutory regulation or exceeds the permitted use, you will need to obtain permission directly from the copyright holder. To view a copy of this licence, visit <http://creativecommons.org/licenses/by-nc-nd/4.0/>.

© The Author(s) 2025